Energy & Environmental Science

Accepted Manuscript

This is an *Accepted Manuscript*, which has been through the Royal Society of Chemistry peer review process and has been accepted for publication.

Accepted Manuscripts are published online shortly after acceptance, before technical editing, formatting and proof reading. Using this free service, authors can make their results available to the community, in citable form, before we publish the edited article. We will replace this *Accepted Manuscript* with the edited and formatted *Advance Article* as soon as it is available.

You can find more information about *Accepted Manuscripts* in the Information for Authors.

Please note that technical editing may introduce minor changes to the text and/or graphics, which may alter content. The journal's standard Terms & Conditions and the Ethical guidelines still apply. In no event shall the Royal Society of Chemistry be held responsible for any errors or omissions in this *Accepted Manuscript* or any consequences arising from the use of any information it contains.

ROYAL SOCIETY OF CHEMISTRY

www.rsc.org/ees

Scalable Fabrication of Micron-Scale Graphene Nanomeshes for High-Performance Supercapacitor Applications

Hyun-Kyung Kim, [1,2] *Seong-Min Bak,* [3] *Suk Woo Lee,* [1] *Myeong-Seong Kim,* [1] *Byeongho Park,* [4] *Su Chan Lee,* [4] *Yeon Jun Choi,* [1] *Seong Chan Jun,* [4] *Jung Tark Han,* [5] *Kyung-Wan Nam,* [6] *Kyung Yoon Chung,* [7] *Jian Wang,* [8] *Jigang Zhou,* [8] *Xiao-Qing Yang,* [3] *Kwang Chul Roh,** [9] *and Kwang-Bum Kim** [1]

[1] Department of Materials Science and Engineering, Yonsei University, 134 Shinchon-dong, Seodaemoon-gu, Seoul 120-749, Republic of Korea

[2] Department of Materials Science and Metallurgy, University of Cambridge, 27 Charles Babbage Road, Cambridge CB3 0FS, United Kingdom

[3] Chemistry Department, Brookhaven National Laboratory, Upton, NY 11973, USA

[4] School of Mechanical Engineering, Yonsei University, 134 Shinchon-dong, Seodaemoon-gu, Seoul 120-749, Republic of Korea

[5] Nano Carbon Materials Research Group, Creative and Fundamental Research Division, Korea Electrotechnology Research Institute, Changwon 642-120, Republic of Korea

[6] Department of Energy and Materials Engineering, Dongguk University, Seoul, 26 Pil-dong, 3-ga, Jung-gu, Seoul 100-715, Republic of Korea

Energy & Environmental Science Accepted Manuscript

[7] Center for Energy Convergence Research, Korea Institute of Science and Technology, Hwarangno 14-gil 5, Seongbuk-gu, Seoul 136-791, Republic of Korea.

[8] Canadian Light Source Inc., Saskatoon, Saskatchewan S7N 0X4, Canada

[9] Energy Efficient Materials Team, Energy & Environmental Division, Korea Institute of Ceramic Engineering & Technology, 101, Soho-ro, Jinju 660-031, Republic of Korea

Energy & Environmental Science Accepted Manuscript

Abstract

Graphene nanomeshes (GNMs) with nanoscale periodic or quasi-periodic nanoholes have attracted considerable interest because of unique features such as their open energy band gap, enlarged specific surface area, and high optical transmittance. These features are useful for applications in semiconducting devices, photocatalysis, sensors, and energy-related systems. Here, we report on the facile and scalable preparation of multifunctional micron-scale GNMs with high-density of nanoperforations by catalytic carbon gasification. The catalytic carbon gasification process induced selective decomposition on the graphene adjacent to the metalcatalyst, thus forming nanoperforations. The pore size, pore density distribution, and neck size of the GNMs can be controlled by adjusting the size and fraction of the metal oxide on graphene. The fabricated GNM electrodes exhibit superior electrochemical properties for supercapacitor (ultracapacitor) applications, including exceptionally high capacitance (253 F g^{-1} at 1 A g^{-1}) and high rate capability (212 F g^{-1} at 100 A g^{-1}) with excellent cycle stability (91% of the initial capacitance after 50,000 charge/discharge cycles). Further, the edge-enriched structure of GNMs plays an important role in achieving edge-selected and high-level nitrogen doping.

Energy & Environmental Science Accepted Manuscript

Introduction

Graphene nanomeshes (GNMs) are novel graphene structures with a high density of nanoscale perforations (holes or pores) on the conjugated carbon surface.[1-5] GNMs exhibit quantum confinement, enriched edge and localization effects, combined with the inherent properties of graphene, and thus, they have great potential applications in the fields such as energy storage, gas separation/storage, and magnetic, optical, and electronic devices.[1-7] Further, compared to the basal planes in normal graphene sheets, the nanoscale periodic or quasi-periodic nanoholes within GNMs possess more active sites and an open porous structure for faster electron transport and higher electrocatalytic activity.[6,7] Substantial effort has been devoted to tailoring graphene sheets into a confined geometry similar to that of nanoribbons and quantum dots and to doping of heterogeneous atoms into the graphene material.[5-10]

The major challenge in fabricating GNMs is increasing the density of nanoholes per unit area such that the neck width of pores is ≤20 nm.[2,3] Many approaches for obtaining these delicate structures using graphene films as the starting material have been proposed, such as lithography (including electron beam, block copolymer, and nanosphere), ion irradiation, hydrothermal approaches, templates, chemical vapor deposition, and plasma etching.[1-7,11,12] However, such methods have extremely low yields and involve difficult handling, and hence, there is a need for a new scalable synthetic method.

The most widely used method for preparing graphene on a large scale at low cost involves the reduction of graphite oxide (GO).[13-15] There have been attempts to synthesize GNMs using GO or reduced graphene oxide (RGO), which can be cheaply produced on a large scale and processed using wet approaches. However, most of the resulting materials had non-uniform (or irregular) pore formations, and therefore do not exhibit the intrinsic special properties of

Energy & Environmental Science Accepted Manuscript

GNMs.[15,16-20] The development of a facile, advantageous methods for preparing GNMs with integrated functionalities and intrinsic properties remains a challenge.

Further, studies thus far have mainly explored the electronic properties of GNMs, such as Fermi level change and band-gap opening, by inducing changes in their electronic structure.[5-7,11,12] However, graphene has recently received intensive interest as a new supercapacitor electrode material because of its high intrinsic properties.[24-32] Especially, GNMs have many additional properties that are assumed to be closely associated with their electrochemical properties, especially quantum confinement and edge effects,[21,23] and the nanoperforations on graphene may contribute to the improved ionic transport rate.[16,20] Thus, studies investigating GNMs as possible electrode materials for electrical energy storage devices are urgently needed.

Herein, we explored scalable synthetic methods and specific applications of GNMs, which are micron-scale nanoperforated graphene sheets prepared from GO by catalytic carbon gasification. These GNMs were scalable and multifunctional, and the neck size could be controlled to widths as small as 10 and 20 nm. Moreover, GNM-based supercapacitors displayed superior electrochemical properties, including exceptionally high rate capability, high frequency response, and excellent cycle stability. The unique morphology of the GNMs could be the subject of extensive useful research and technology development.

Energy & Environmental Science Accepted Manuscript

Results and Discussion

GNMs were synthesized from GO through catalytic carbon gasification using metal oxide nanoparticles obtained in situ to create nanoperforations, as shown in Figure 1. First, catalytic metal oxide (SnO_2) nanoparticles were deposited onto the GO surface using an aqueous-solution-based regular deposition process developed in our laboratory.[33] In this process, nanoscale metal oxides were homogeneously synthesized on RGO surface to act as catalysts for carbon gasification. Next, the composites were subjected to controlled air oxidation via heating in a tube furnace. The catalytic carbon gasification process induced selective decomposition on the graphene adjacent to the SnO_2 (nanocatalysts) at temperatures lower than the carbon combustion temperature, thus forming nanoperforations corresponding to the metal oxide sizes and distribution on the carbon surface.[37-39] Finally, to remove the catalysts, the SnO_2/SnO-RGO sheets were refluxed at 80 ℃ with diluted acid (HI, 1 M) for 4 h to obtain the GNMs. In this process, HI not only etched the metal oxide but reduced the GO.[38] The formation of nanoperforations on graphene was also confirmed by SEM (Figure S1, ESI).

To validate the creation of nanoperforations by catalytic carbon gasification in situ, decomposition of SnO_2-RGO was performed in the TEM chamber (Figure S2, ESI) to observe the pore formation process under similar conditions including temperature and O_2 gas flow with rapidly increasing temperature using current density as the energy provider. Images were recorded (x4) between 100 and 350 ℃, and at approximately 350 ℃, we observed the creation of nanoperforations on the RGO near the SnO_2 nanoparticles (Figure S2 and Movie S1, ESI). Futher evidence for the introduction of nanopores on RGO sheets via catalytic carbon decomposition was provided by TG/DSC and Py-GC/MS (Figure S3 and S4). As shown in Figure S3, P-graphene clearly began to decompose when the temperature was approximately

Energy & Environmental Science Accepted Manuscript

500 °C (exothermic peak in DSC), and it completely decomposed from C to CO or CO_2. However, SnO_2-RGO decomposed at a lower temperature (approximately 450 °C). These observations indicate that the SnO_2 nanoparticles catalyzed the oxidation of RGO that was in contact with them. The decomposition temperature decreased with increased amounts of SnO_2 (See Figure S5, ESI). Corresponding profiles for carbon monoxide (CO, m/z = 28) and carbon dioxide (CO_2, m/z = 44) gas release were obtained under the same experimental conditions using Py-GC/MS. Similarly to the TG/DSC results, during catalytic carbon gasification, CO and CO_2 release peaks were observed for P-graphene and SnO_2-RGO at 470 °C and 430 °C, respectively, and sudden gassing of SnO_2-RGO was observed in the MS profile.

The nanoperforations on the GNMs were observed using TEM and AFM (Figure 2 and Figure S6); images of P-graphene are shown in Figure S6. The perforations on the RGO nanosheets were 5–10 nm in size and were on the micron scale, as shown in Figure 2a-d and Figure S7. The correction of spherical aberrations (Cs) TEM technique was used to clearly observe the nanoperforations (Fig. 2d) and the Fast Fourier Transform (FFT) diffraction patterns (inset of Figure 2d) of nonperforated regions in the GNMs. The FFT diffraction patterns were calculated using a digital micrograph software. The FFT diffraction patterns of nonperforated areas showed distinct hexagonal patterns similar to those of typical unmodified (e.g., highly conductive RGO or CVD graphene) graphene.[41,42] The diffraction patterns also showed a single set of hexagons, suggesting that the local area was a perfectly crystallized graphene monolayer. However, broad FFT patterns were observed in the nanoperforated area, suggesting defects, wrinkles, or rotational stacking, as shown in Figure S8. These results confirm that highly crystalline graphitic structures remained on the GNM sheets except in the nanoperforated areas. We determined the size of the perforations on the GNMs using AFM, as shown in Figure 2e. Nanoperforations are

Energy & Environmental Science Accepted Manuscript

clearly seen on the GNM sheets, unlike on P-graphene (See Figure S9, ESI), indicating the formation of pores. The height profile diagram indicates the average size of the perforations (5–10 nm) on the graphene sheets.

By using the catalytic carbon gasification method to generate the nanoperforations, the pore density distribution could be controlled from 500 to 5000 μm^{-2} of GNMs using 7 wt.% SnO_2-RGO (L-GNMs), 11 wt.% SnO_2-RGO (GNMs), and 17 wt.% SnO_2-RGO (H-GNMs) (Figure 3 a-c and Figure S1, ESI). Additionally, to investigate the applicability of other materials for formation of GNMs, Fe_3O_4 and RuO_2[43,44] were used as the catalytic metal oxides instead of SnO_2 on RGO. We were able to successfully prepare GNMs by this catalytic carbon gasification method (See Figure S10, ESI), by which the size of the perforations (~5 nm and ~20 nm using RuO_2 and Fe_3O_4) on RGO can be controlled.

The GNMs were characterized by XRD at all stages of production (Figure 4a). Acid-mediated oxidation of GO is indicated by the (002) peak at $2\theta = 10.3°$ and occurred due to the insertion of -COOH, -OH, and epoxy functionalities between the graphene sheets of graphite,[13-15,41] increasing the d-spacing in GO by 0.83 nm. A new broad band in the graphitic region at about $2\theta = 24°$ (d-spacing ~3.6 Å) is clearly seen for the GNMs, supporting the substantial removal of oxygen-containing functionalities. In addition, the disappearance of SnO_2 peaks (JCPDS 72-1147)[31] from these samples confirmed the complete removal of the metal oxide. Compared with those of the parent GO, the GNM peaks were dramatically upshifted, suggesting that the GNMs were well-ordered with two-dimensional sheets and that there was a decrease in the average interlayer spacing of the GO.[41,42]

The chemical composition, bonding nature, and structural change of each sample (GO, SnO_2-RGO, and GNMs) were characterized by XPS, NMR, and Raman spectra. As shown in Figure 4b,

Energy & Environmental Science Accepted Manuscript

the as-synthesized and reduced GO were analyzed using XPS to observe the evolution of the oxygen functional groups. SnO_2-RGO showed slightly reduced oxygen peaks and Sn $3d_{5/2}$ and Sn $3d_{3/2}$ peaks. The ratio of the C 1s and O 1s peak areas confirmed that the increased C 1s corresponded to a prominent carbon peak from GO (C contents: 65.3 at.% and O contents: 34.6 at.%) to GNMs (C contents: 86.9 at.% and O contents: 13.1 at.%), indicating replacement of the oxygen.[13,28] As shown in the C 1*s* XPS spectra (See Figure S11) of SnO_2-RGO and GNMs, the proportion of carbon–carbon (C–C) bonds increased and the intensity of the C–OH peak decreased with the removal of SnO_2 and the reduction of graphene by HI treatment of the GNMs. In the Sn 3D XPS spectra, the Sn $3d_{5/2}$ and Sn $3d_{3/2}$ peaks associated with the SnO_2 nanoparticles are located at 487.5 and 495.9 eV,[45] suggesting the coupling of the SnO_2 nanoparticles with the RGO sheets. Moreover, during the catalytic carbon gasification and the subsequent acid treatment, the amount of C–OH and C–O–C groups on the GNMs was significantly lower than that expected based on the intensity of the peak at 533.4 eV in the GO O 1*s* spectrum. This finding also suggests that the hydrogen in the hydroxyl groups was reduced during the process.[33] The solid state ^{13}C MAS NMR spectra indicated that the catalytic carbon gasification and acid treatment induced significant structural changes in GNMs from GO (Figure 4c). The spectra revealed a decrease in the oxygen functional groups at 168.71 (O = C–O), 68.41 (C–OH), and 60.01 (C–O–C) ppm for GO, as well as new broad resonance peaks at 116.35 and 110.50 ppm (graphitic, C sp^2) for SnO_2-RGO and GNM, respectively, similar to those reported for RGO and graphene.[46,47-49] Graphitic C sp^2 peaks appeared at 127.75 ppm for GO, at 116.35 ppm for SnO_2-RGO, and at 110.50 ppm for GNM. These results indicate that the graphitic structure of the GNMs had already been substantially restored by the formation of aromatic pyrazine rings at the edges during the catalytic carbon gasification and acid treatment. The change in the D/G

Energy & Environmental Science Accepted Manuscript

intensity ratio of the Raman spectra for GNMs and that of P-graphene indicated the introduction of edge sites by nanoperforations on the graphene sheets. Raman spectroscopy is widely used to characterize carbon products, especially because conjugated and double carbon–carbon bonds lead to high Raman intensities. Raman spectra reveal two prominent peaks: the D band (1346 cm^{-1}) and the G band (1597 cm^{-1}). The D peak indicates the introduction of defects or imperfections in the graphitic domain, and the G peak indicates that the graphitic domain is well maintained. The ratio of the D and G peaks is used to determine the graphitic structure intensity.[33,46,47] Fig. 4d shows the Raman spectra of GO, SnO_2-RGO, and GNM. The calculated D/G ratios for GO, SnO_2-RGO, and GNMs were 0.9, 0.97, and 1.05, respectively. The large D/G ratio for the GNMs is attributed to the introduction of defects in the graphitic domain during preparation. This finding was further confirmed by large-scale Raman mapping (See Figure S12). In the Raman mapping data, the color gradient bars at the right of each map and the scale bars are equivalent to 30 μm for graphene and GNM. Differences in the D/G ratio for P-graphene, GNMs, and H-GNMs (from the above-mentioned perforation density of GNM) are indicated by color differences. The color differences between the four Raman maps are clear; thus, the high D/G ratio and the strong color in the maps confirm that GNMs have a higher density of edge sites (or defect sites) than P-graphene.

Additionally, to compare P-graphene with GNMs, we performed a gas adsorption measurement to investigate the specific surface area and pore size distribution P-graphene and GNMs. The N_2 adsorption−desorption isotherms (See Figure S13) show a large hysteresis loop for P-graphene at relative vapor pressures of 0.4−0.8, which are characteristic features of a type IV isotherm; the pore structure was expected to originate in the typical RGO flakes.[41] In contrast, the GNMs exhibited a Type I isotherm with some characteristics of a Type IV isotherm. That is,

Energy & Environmental Science Accepted Manuscript

obvious micropore filling occurred at very low relative pressure, and the adsorption process quickly reached a well-defined plateau.[50] A very small but identifiable hysteresis loop indicates the presence of a limited amount of mesopores. The presence of macro- and mesopores in the GNMs, which had a relatively large specific surface area and high porosity, should allow for greater material–electrolyte contact area and promote the diffusion of ions for energy storage applications. The BET surface areas were 210 $m^2 g^{-1}$, with pore volume of 0.21 $cm^3 g^{-1}$ (P-graphene) and 261 $m^2 g^{-1}$ (GNMs), with pore volume of 0.25 $cm^3 g^{-1}$.

The UV–vis spectra and PL excitation measurements for P-graphene and the GNMs shown in Figures S14a reveal that the electronic structure of the GNMs changed from the nanoperforations on the graphene and that the GNMs showed lower absorbance values than P-graphene owing to the nanoperforations on the graphene sheets. Further, the GNMs had two peaks at 227 and 275 nm, which were generated by excitons in the graphene sheet. Similar to silicon nanocrystals, quantum confinement effects arising from the nanoperforations on the graphene resulted in discrete spectra and remarkable absorbance peaks.[8] The PL of the GNMs was investigated using fluorescence spectrophotometry at an emission wavelength of 458 nm (Figure S14b). The PL intensity of edge-bound, nanometer-sized graphene generally presents distinctive properties owing to quantum confinement and edge effects. The small neck width (10~20 nm) of GNMs played a role in the quantum confinement effect and led to enhanced PL emission with increasing quantum yield. The GNMs showed three high-intensity peaks at 382, 433, and 668 nm, whereas P-graphene showed one small emission peak at 433 nm, which is typical RGO samples.[8,9] The enriched edges of nanoperforated GNMs had various functional groups such as carbonyl, carboxyl, phenol, and quinone, which generated defect levels between the band gap. Electron transition through the defect levels contributed to the radiation of low-energy photons at

Energy & Environmental Science Accepted Manuscript

a wavelength of 668 nm. Typically, graphene-based materials have emissions between 400 and 500 nm. However, the GNMs showed blue-shifted emissions at 382 nm with high-energy photons because the band gap enlarged as quantum confinement improved owing to nanoholes on the graphene surface. The fluorescence images in the inset of Fig. S14b were measured from graphene and GNMs using an optical microscope with a UV excitation beam. GNMs showed greater fluorescence than P-graphene and, specifically, blue and violet fluorescence was observed with a strong PL peak at 400 nm (Figure S14b) owing to quantum confinement and edge effects.[10]

Figure 5 shows the electrochemical properties of GNMs and P-graphene as electrode materials for supercapacitor applications. Each material exhibited typical rectangular cyclic voltammograms (CV) without distinct peaks in the potential window between 0 and 2.7 V in the $TEABF_4$/ACN electrolyte, indicating that the current response was primarily a result of EDL formation without pseudocapacitive behavior at the interface between the electrode materials and the electrolyte ions. CV (Figure 5a and Figure S15, ESI) and galvanostatic charging–discharging (GCD, Figure 5b) revealed that the electrochemical performance of GNMs were superior to that of P-graphene. The nearly rectangular CV curves at a high scan rate of 1,000 mV/s and the nearly triangular charge/discharge curves at a high current density of 100 A/g indicate nearly ideal electrical-double-layer capacitive behavior and efficient electrolyte ion transport throughout the GNM electrodes.[25-27] GNMs delivered higher current responses and higher specific capacity than P-graphene. Both GNMs and P-graphene showed linear GCD profiles at various current densities between 1 and 20 A/g, indicating typical EDL capacitive behavior (Figure 5b and c). The specific capacitance (C_{sp}) of a single electrode was obtained from discharge profiles using the following equation:[23]

Energy & Environmental Science Accepted Manuscript

$$C_{sp} = I \times \Delta t / V, \quad \text{(Eq. 1)}$$

where Δt, V, and I represent the discharge time, potential window, and applied current density per unit mass of a single electrode, respectively. The GNMs delivered high specific capacitances of 253, 250, 245, and 237 F/g at current densities of 1, 2, 5, and 10 A/g, respectively. The specific capacitance remained at 212 F/g even at a high current density of 100 A/g, corresponding to an 84 % retention of the specific capacitance measured at 1 A/g. In contrast, graphene exhibited relatively low specific capacitances of 158, 154, 146, and 130 F/g at current densities of 1, 2, 5, and 10 A/g, respectively, in the same electrolyte. These results confirmed that the specific capacitance and rate capability of the GNMs were much higher than those of P-graphene. Additionally, the packing density of GNMs was 0.54 g cm^{-3}, which is slightly higher than that of P-graphene (0.38 g cm^{-3}) owing to abundant in-plane nanopores, good dispersity, and processability.[15,31,51] Although the volumetric capacitance of GNMs is lower than gravimetric capacitance (Figure S16), it has a similar packing density to that of activated carbon materials (0.4–0.7 g cm^{-3}) for commercial supercapacitor applications.[51] Figs. 5d and e show the Nyquist and Bode plots, respectively, obtained from EIS analysis of the GNMs and graphene electrodes. The point at which the plot intersects the real axis in the Nyquist plot (Figure 5d) corresponds to the equivalent series resistance, which represents the ionic resistance of the electrolyte and the electrical conductivity of the electrode.[28,29] The GNM electrode exhibited a shorter semicircle with a smaller diameter than that of P-graphene, indicating lower charge transfer resistance and more efficient electrolyte diffusion within the GNM electrode. On the real axis, the equivalent series resistance (Rs) of the GNMs (0.97 Ω) was lower than that of P-graphene (1.33 Ω). Notably, the equivalent series resistance (ESR) is related to both the electrical resistance of the electrodes and ion diffusion resistance in the electrodes. Although the conductivity of P-graphene was

Energy & Environmental Science Accepted Manuscript

slightly better than that of the GNMs, the GNMs showed much better ion diffusion, which led to a lower ESR. The Bode plot in Figure 5e provides useful insight into the rate capability of carbonaceous materials.[21] A maximum is observed at a characteristic frequency (f_0); the reciprocal of this frequency represents the minimum time, which is referred to as the time constant (t) that can be used for charging or discharging the electrode while maintaining good capacitive behavior. The time constant for the GNMs was 0.59 s (f_0= 1.68 Hz), which was lower than that for P-graphene (τ =0.94 s; f_0= 1.06 Hz), indicating that GNMs showed better rate capability. This finding is consistent with the rate capability measured in the GCD test (Figure 5c). The GNMs exhibited excellent cycling stability in the $TEABF_4$/ACN electrolyte, retaining 91% of the initial capacitance after 50,000 charge/discharge cycles at a high current density of 10 A/g (Figure 5f). The excellent electrochemical properties of the GNM electrodes were also evident in the three-electrode half cell test in $LiPF_6$ in EC/DMC (1:1, v:v) (See Figure S17, ESI).

These studies indicate that GNM electrodes not only exhibited much higher specific capacitance than P-graphene electrodes but also showed excellent rate capability and capacitance retention at high charging/discharging rates, which can be attributed to increased ion-accessible surface area due to the perforations and the enriched edge sites of the GNMs. Nanoperforations on graphene act as fast ion/electrolyte transport paths, alleviating the close-stacking problem of RGO.[16-18] Therefore, the increased ion-accessible surface area of GNMs led to faster ion transport. Furthermore, the capacitance of edge sites is several times that of the basal plane.[19,21,22] Nanoperforations on graphene introduce more edge sites, endowing the graphene with greater capacitance (via increased ion storage) and making it more chemically active than P-graphene. Thus, a systematic understanding of the nature of edges, through both theory and experiments, is

Energy & Environmental Science Accepted Manuscript

critical for improving the electrochemical performance of graphene-based materials in energy storage devices.

Heterogeneous atom doping is a key approach to the chemical functionalization of graphene that mainly alters its electrical properties. Elements in the third or fifth group, such as nitrogen and boron, are usually used as dopants. Well-bonded nitrogen atoms improve the electron conductivity and increase the number of active sites (defects). [52] Therefore, nitrogen doping is an effective method for improving both the microstructure and electrical properties of graphene.

Figure 6a shows the full-scale XPS spectra of nitrogen-doped GNMs (N-GNMs) prepared by NH_3 gas treatment of GNMs at 900 °C. Compared with the XPS data for the GNMs (Fig. 6b), the new peak appearing at a binding energy of approximately 400 eV (N 1s) for N-GNMs confirmed that nitrogen was successfully doped into the carbon structure. The nitrogen content of N-GNMs was calculated as 6.19 at.%, greater than that of N-doped graphene (NG) without nanoperforations (4.42 at.%). It is known that the oxygen-containing functional groups in GO, including the carbonyl, carboxylic, lactone, and quinone groups, react with NH_3 to form C–N bonds.[53] Similarly, oxygen groups at the edge and defect sites in the basal plane of graphene (or RGO) could be preferred reaction sites for NH_3.[54] In the present study, we believe that the edge-enriched structure of GNMs played a pivotal role in achieving a higher nitrogen-doping level for N-GNMs than for NG. Evidence to support this hypothesis is present in the high-resolution XPS spectra of the N 1s region (Figure 6b), which showed a larger proportion of 'edge-N' such as pyridinic (ca. 398.1 eV) and pyrrolic (ca. 399.5 eV) N and a smaller proportion of 'basal-N' (i.e., quaternary N, ca. 401.0 eV), for N-GNMs than for N-G (See Figure S18, ESI). Because GNMs exhibit a high density of edges and defects (i.e., perforations) on the basal plane, more pyridinic and pyrrolic N were generated than quaternary N.

Energy & Environmental Science Accepted Manuscript

This finding was further supported by NEXAFS spectroscopy, which can provide detailed information about the electronic structure of carbon-based materials. Figure 6c shows the C K-edge NEXAFS spectra for GNMs and N-GNMs. The two main peaks near 285 and 292 eV for both samples are attributed to transitions from C 1s to unoccupied states with π* C=C and σ* C-C characteristics, respectively. Regarding the GNM spectra, the peak observed in the intermediate energy range between π* and σ* resonance can be attributed to transitions from core levels into σ*C-O (ca. 288.2 eV) and π* C=O (and/or O=C-O, ca. 289.5 eV) bonds localized at oxygen functional groups on GNM.[55,56] A close examination of the peaks near the π* resonances for both samples (Figure 6c, inset) reveals two notable changes: 1) the appearance of a new peak at approximately 287.2 eV, which indicates the transition to antibonding states of C-N bonds[56-58] by the incorporation of nitrogen into the GNM structure, and 2) a decrease in the peak intensity of the π* C=O transition due to the reduction of C=O bonds upon NH_3 treatment. Interestingly, in contrast to the significant change in peak intensity of the π* C=O transition, only a small change was observed for the peak of the σ*C-O transition. Because the C=O bonds are mainly derived from carboxyl groups (-COOH) thought to reside at the edges and in interior holes (i.e., nanoperforations), the diminution of the C=O resonance in N-GNMs implies a site-selective nitrogen doping reaction between edge carboxyl groups and NH_3. The dominant role of carboxyl groups at edge sites in the GNMs in accepting nitrogen atoms is in accord with both the findings of the XPS analysis (Figure 6b) and with previous reports.[55,59,60] In addition, the relative intensities of the π* and σ* resonances (I_{π^*}/I_{σ^*}) increased slightly with NH_3 treatment, suggesting partial restoration of the π-conjugation.[54,56]

Figure 6d displays the O K-edge NEXAFS spectra with pre-edge normalization, which allows comparison of the relative oxygen content in GNMs and N-GNMs. The peak near 533 eV was

Energy & Environmental Science Accepted Manuscript

assigned to π* C=O resonance, which may have belonged to carboxyl groups attached at edges and nanoperforations, and likely belonged to carbonyl groups bonded to an aromatic ring.[60,61] The peak near 536 eV originated from the π* C-O resonance in epoxides, and the peak above ~540 eV was assigned to σ* C-O resonance.[62,63] The edge jump intensity at 570 eV, beyond the σ* feature, reflected the total oxygen content of the samples.[54,55] As shown in Figure 6d, the total oxygen content from the oxygen functional groups on GNMs substantially decreased during the NH_3 treatment. These observations confirm that the reduction of GNMs was caused by nitrogen doping and are in accord with the C K-edge spectra results above. Notably, the π* C=O resonance was diminished more than the π* C-O resonance upon nitrogen doping, indicating site-selective nitrogen doping at edges and nanoperforations, as noted above for the C K-edge NEXAFS and XPS results.

To probe the local electronic and geometric structure near nitrogen atoms in N-GNM, the N K-edge NEXAFS spectrum was analyzed and deconvoluted (Figure 6e). In contrast to the overlapping peaks in the XPS analysis (Figure 6a), the well-resolved features observed in the NEXAFS spectra provided more reliable evidence for the different local bonding environment of N.[54] The three resonance peaks at 400, 401.6, and 403.1 eV were ascribed to pyridinic (N-6), pyrrolic (N-5), and quaternary (N-Q) sites, respectively.[54] The broad resonance centered at approximately 408 eV was attributed to the transition from the N 1s core level to a σ* state localized on C–N bonds.[54,55] Similarly to the XPS data (Figure 6b), 'edge-N' at N-6, N-5 sites appeared more frequently than 'basal-N' at N-Q sites.

A single N-GNM sheet supported on a holey carbon TEM grid was characterized using STXM image stacks obtained at the C K-edge (280-320 eV) and the N K-edge (395-430 eV). The overall morphology of the single N-GNM sheet is shown in Figure S19a; the vertical gray scale

Energy & Environmental Science Accepted Manuscript

represents the optical density (OD, i.e., absorbance), which is related to the absolute thickness of the sample region. The color composite map (Figure S19b) was generated from the average OD image by combining individual component maps (Figure S19c-j, see caption for Figure S19) using principal component analysis, and the corresponding C and N K-edge NEXAFS spectra (Figure S19k and i, respectively) were derived from the same regions. One notable feature is that the C K-edge spectra for the individual N-GNM components (i.e., Figure S19f–j) showed strong π* C=C intensities even in the flat, thin central region (Figure S19f). Because the STXM measurements were performed at normal incidence using polarized soft X-ray radiation, based on the dipole selection rule, an orbital with perpendicularly symmetric orientation to the basal plane of the N-GNMs (π* C=C) should not be resonant. Therefore, the pronounced π* C=C feature at approximately 285 eV on the C K-edge spectra corresponded to a distinctive corrugation or ripple in the N-GNM structure.[55,58] This may have been due to distortion of the graphene structure caused by defects on basal planes introduced by the nanoperforations. Regarding the N K-edge, the color map (Figure S19b) and spectra (Figure S19i) indicate that nitrogen doping was consistent throughout the GNM framework.

GNMs possess many intrinsic properties such as edge sites, perforations, and quantum confinement effects; these properties can change the electric properties of graphene and enhance many other properties. Additionally, the presence of heterogeneous atoms in graphene at edges and in basal planes influences the local electronic structures, enhancing binding with ions in solutions. Because edge sites are much more chemically active than those within the plane of P-graphene, they are very useful for heterogeneous doping of graphene.

In particular, GNMs were prepared by catalytic carbon gasification, which allowed control of the perforation density, as shown in Fig 3. We can confirm that the chemical compositions of the

Energy & Environmental Science Accepted Manuscript

as-prepared and N-doped samples (NG, N-(L)-GNMs, N-GNMs, N-(H)-GNMs), as characterized by elemental analysis (EA), and the results are summarized in Table 1. These results confirmed that the oxygen and carbon contents of the L-GNMs and P-graphene were similar, but the GNMs and H-GNMs had a greater density of oxygen (edge sites) than the P-graphene sheets. After N-doping, the nitrogen contents of L-GNMs and NG, N-GNMs were 4.47 wt % and 4.42 wt %, but the N-(H)-GNMs were composed of nitrogen at 4.42 wt % and 6.19 wt %. The performance of the N-doped graphene in supercapacitors is related not only to the nitrogen level, but also to the type of nitrogen. In particular, pyridinic-N and pyrrolic-N play key roles in enhancing the specific capacitance of N-doped materials owing to their pseudo-capacitive contribution, while quaternary-N could enhance the conductivity of the materials. As shown in figure S20, the N-GNMs had a slightly enhanced specific capacitance and rate capability than that of GNMs electrode. The enhanced electrochemical properties of N-GNMs electrode could be attributed to its very low oxygen content during N-doping process and to the nitrogen-doping effects, by which the recovery of the π-conjugated structure in N-GNMs enhances its electrical conductivity. [54] It was demonstrated that the controlled N-doping contents and type of GNMs could be used as promising electrode materials for high performance supercapacitors.

Energy & Environmental Science Accepted Manuscript

Conclusion

In summary, we have demonstrated a simple, inexpensive method for the rapid and scalable production of micron-scale GNMs through nanoperforations, using GO as a starting material. High-resolution TEM analysis of the prepared GNMs indicated the formation of nanoperforations of size 5–10 nm uniformly dispersed on graphene sheets. Furthermore, the neck size of GNMs can be controlled to widths as small as 10–20 nm with pore density distribution of 500–5000 μm^{-2}, by adjusting the size and fraction of metal oxide on graphene. The fabricated GNMs electrodes exhibited superior electrochemical properties, which can be attributed to the increased ion-accessible surface area owing to the perforations and the enriched edge sites of the GNMs. We also present that the edge-enriched structure of GNMs played a pivotal role in achieving edge-selected and/or high nitrogen-doping level for N-GNM. This scalable and robust synthesis method and the novel properties of GNMs presented here greatly advance the potential to launch a vast area of research and technology development.

Energy & Environmental Science Accepted Manuscript

Experimental

Preparation of GNMs To prepare the GNMs series, 1500 mg of GO powder (synthesized using a modification of Hummer's method)[31] was first ultrasonicated in 1500 mL deionized water. Equal amounts of the resulting GO suspension were aliquoted into three identical bottles and then mixed with different weights of $SnCl_2$ powder (98 %, Aldrich) to control the amounts of SnO_2 (7 wt.% SnO_2-RGO and low perforation density (L-) GNMs: 5 mg; 11 wt.% SnO_2-RGO and GNMs: 25 mg; 17 wt.% SnO_2-RGO and high perforation density (H-) GNMs: 75 mg). These mixtures were stirred for 4 h at 25°C. The products were then washed several times with distilled water to remove residual chloride ions and other impurities. Next, the powders were freeze-dried for 24 h. The obtained SnO_2-reduced graphene oxide (RGO) was thermally decomposed at 450 °C for 1 h (two-step process: 25–300 °C (10 ℃/min) and 300–450 °C (3 °C/min) in air. Then, the RGO was immersed in aqueous HI (1 M) and stirred for one day to remove metal-containing species, such as metals and metal oxides. To compare the effects of nanoperforations on graphene, RGO was prepared as above but without metal chloride; this was designated pristine (P-) graphene. To prepare GNMs with Fe_3O_4– or RuO_2–RGO, 500 mg GO in 500 mL diethylene glycol was mixed with 0.25 mg $FeCl_2$ or $RuCl_3$ powder (85 %, Aldrich) under the conditions described above.

To prepare NG (nitrogen-doped P-graphene), N-(L)-GNMs, N-GNMs and N-(H)-GNMs (nitrogen-doped L-GNMs, GNMs and H-GNMs) were placed in an alumina tray and rapidly heated to 900°C for 1 h at a heating rate of 30°C/min under NH_3 gas.

Sample characterization The microstructure of the samples was examined using scanning electron microscopy (SEM, JSM-7001F, JEOL, Ltd.), transmission electron microscopy (TEM,

Energy & Environmental Science Accepted Manuscript

CM200, Philips), and high-resolution transmission electron microscopy (HRTEM, JEM-2100, JEOL, Ltd.). In situ observation was performed using a 300-kV TEM (JEM-3011HR, Jeol Ltd.) with a LaB_6 thermal ion gun at the National Nanofab Center (NNFC). X-ray photon electron spectroscopy (XPS) was performed using an Omicron ESCA Probe (Omicron Nanotechnology, Taunusstein, Germany) with monochromated Al Kα radiation (hν = 1486.6 eV). Raman spectroscopy (Jobin-Yvon LabRAM HR) was performed at 25°C with conventional backscattering geometry and a liquid-N_2-cooled charge-coupled device multichannel detector. A 514.5-nm wavelength argon-ion laser was used as the light source. Solid-satae ^{13}C magic-angle spinning (MAS) nuclear magnetic resonance (NMR) spectra were recorded using a Bruker Avance 500 MHz spectrometer and an MAS probehead with zirconia rotors (diameter, 4 mm). Thermal data were collected using thermogravimetry and differential scanning calorimetry (TG/DSC) and pyrolysis-gas chromatography/mass spectrometry (Py-GC/MS: Py-2020iD, FRONTIER LAB, Japan and 6890N GC/ 5975i MS, Agilent, USA) in air from 25°C to 800°C at the same heating and cooling rates used for sample synthesis. Nitrogen adsorption–desorption isotherms were obtained using a Micromeritics ASAP 2020 physisorption analyzer at 77 K. The surface area was calculated using the Brunauer–Emmett–Teller (BET) method, and the pore size distributions were determined from the desorption branch using the Barrett–Joyner–Halenda (BJH) method. Elemental analysis (Thermo EA1112, Thermo Electron Corp.) was performed to determine the chemical composition of the samples. Absorbance spectra were obtained with a UV–Vis spectrophotometer (JASCO Corporation, V-650). PL of the EuG film samples was investigated using a fluorescence spectrophotometer (PerkinElmer, LS-55) and a fluorescence microscope (Olympus, IX 71 (IX2 series)). Near edge X-ray absorption fine structure (NEXAFS) spectroscopy was performed at the spherical grating monochromator (SGM) beamline of the

Energy & Environmental Science Accepted Manuscript

Canadian Light Source. Powder samples were mount on the indium foil. NEXAFS data were recorded using the surface-sensitive total electron yield (TEY) method with specimen current. TEY data were first normalized by the incident photon flux I_0 measured with a gold mesh and refreshed at the SGM prior to measurement. The incident beam was set at the magic angle (54.7°) relative to the sample to eliminate preferential orientation effects. The C and N K-edge spectra were processed using the pre- and post-edge normalization method[32] and were performed using the Athena program.[33] The O K-edge spectra were only pre-edge normalized to allow evaluation of the relative oxygen content at 570 eV, beyond the σ* feature. The N-GNM powder was sonically dispersed on a TEM grid (Cu grid with holey carbon) for scanning transmission X-ray microscopy (STXM). STXM experiments were performed on the SM beamline at CLS, and the data were analyzed using aXis2000 software (http://unicorn.mcmaster.ca/aXis 2000.html). The C K-edge image stack covered an energy range of 280–320 eV with energy steps of 0.15 eV. The N K-edge image stack covered an energy range of 395–430 eV with energy steps of 0.2 eV. The image pixel size was 40 nm with a 1 ms dwell time per pixel. Spatially resolved NEXAFS spectra for different regions of interest were extracted from the aligned image stacks using image masks. Details of the STXM experimental and data analysis procedures can be found elsewhere.[34]

The electrochemical properties of the P-graphene, GNMs, and N-GNMs electrodes were investigated by using a CR2032 coin cell at room temperature. Each electrode was prepared by using a slurry composed of 90 wt.% of the active materials (P-graphene, GNMs and N-GNMs) and 10 wt.% of polyvinylidene fluoride (PVDF; Aldrich) as a binder dissolved in N-methylpyrrolidone (NMP). The 0.9-1 mg slurry was uniformly cast on an etched aluminum foil by using a doctor blade and then dried in a vacuum oven at a temperature of 100 ℃ for 24 h. A

Energy & Environmental Science Accepted Manuscript

2032 coin cell, which was a symmetrical two-electrode unit cell, was assembled with an area of 1.13 cm^2 and a microporous polyethylene film (Celgard 2400) separator in an argon filled glove box. The electrolyte was 1M tetraethyl ammonium tetrafluoroborate ($TEABF_4$) dissolved in acetonitrile (ACN) or 1M Lithium hexafluorophosphate ($LiPF_6$) in ethylene carbonate/dimethyl carbonate (EC/DMC; 1:1 v/v). Charge–discharge tests and CV were performed by using a potentiostat/galvanostat (VMP3, Princeton Applied Research). In addition, EIS measurements were performed by using the coin cell and the same potentiostat/galvanostat at alternating current (AC) frequencies in the 200 kHz to 10 mHz range at a 10 mV AC amplitude.

Energy & Environmental Science Accepted Manuscript

References

1. J. W. Bai, X. Zhong, S. Jiang, Y. Huang and X. F. Duan, *Nat. Nanotechnol*. 2010, **5,** 190-194.
2. Z. Y. Zeng, et al. *Adv. Mater.* 2012, **24,** 4138-4142.
3. Y. Zhao, et al. *Energ. Environ. Sci.* 2014, **7,** 1913-1918.
4. V. H. Nguyen, F. Mazzamuto, J. Saint-Martin, A. Bournel and P. Dollfus, *Nanotechnology* 2012, **23,** 289502-289503.
5. J. Yang, et al. *Nanoscale* 2014, **6,** 13301-13313.
6. D. P. Yang, et al. *J. Phys. Chem. C* 2014, **118,** 725-731.
7. O. Akhavan, *ACS Nano* 2010, **4,** 4174-4180.
8. J. Lu, et al. *ACS Nano* 2009, **3,** 2367-2375.
9. F. Liu, et al. *Adv. Mater.* 2013, **25,** 3657-3662.
10. Y. W. Son, M. L. Cohen and S. G. Louie, *Phys. Rev. Lett.* 2006, **97,** 216803-216806.
11. J. Lee, et al. *Nano Lett.* 2012, **12,** 6078-6083.
12. J. H. Shen, Y. H. Zhu, X. L. Yang and C. Z. Li, *Chem. Commun.* 2012, **48,** 3686-3699.
13. H. A. Becerril, et al. *ACS Nano* 2008, **2,** 463-470.
14. S. F. Pei and H.-M. Cheng, *Carbon* 2012, **50,** 3210-3228.
15. X. Zhao, C. M. Hayner, M. C. Kung and H. H. Kung, *ACS Nano* 2011, **5,** 8739-8749.
16. D. Zhou, Y. Cui, P. W. Xiao, M. Y. Jiang and B. H. Han, *Nat. Commun.* 2014, **5,** 4716-4722.
17. J. G. Radich and P. V. Kamat, *ACS Nano* 2013, **7,** 5546-5557.
18. R. Mukherjee, A. V. Thomas, A. Krishnamurthy and N. Koratkar, *ACS Nano* 2012, **6,** 7867-7878.

Energy & Environmental Science Accepted Manuscript

19. Yi Lin, K. A. Watson, J. Kim, D. W. Baggett, D. C. Working and J. W. Connell, *Nanoscales* 2013, **5,** 7813-7824.

20. Yi Lin, X. Han, C. J. Campbell, J. Kim, B. Zhao, W.i Luo, J. Dai, L. Hu and J. W. Connell, *Adv. Funct. Mater.* 2015, **25**, 2920–2927.

21. S. Banerjee, et al. *ACS Nano* 2013, **7,** 834-843.

22. W. J. Yuan, et al. *Sci. Rep.* 2013, **3,** 2248-2253.

23. H. C. Youn, et al. *ChemSusChem* 2015, **8,** 1875-1884.

24. J. H. Lee, et al. *ACS Nano* 2013, **7,** 9366-9374.

25. M. D. Stoller, S. J. Park, Y. W. Zhu, J. H. An and R. S. Ruoff, *Nano Lett.* 2008, **8,** 3498-3502.

26. Y. W. Zhu, et al. *ACS Nano* 2010, **4,** 1227-1233.

27. Q. Cheng et al. *Phys. Chem. Chem. Phys.* 2011, **13**, 17615-17624.

28. Z. B. Lei, N. Christov and X. S. Zhao, *Energ. Environ. Sci.* 2011, **4,** 1866-1873.

29. K. X. Sheng, Y. Q. Sun, C. Li, W. J. Yuan and G. Q. Shi, *Sci. Rep.* 2012, **2,** 247.

30. X. G. Han, et al. *ACS Nano* 2014, **8,** 8255-8265.

31. Y. X. Xu, et al. *Nat. Commun.* 2014, **5,** 4554-4561.

32. Z. J. Fan, et al. *Carbon* 2012, **50,** 1699-1703.

33. H. K. Kim, et al. *Chem. Mater.* 2014, **26**, 4838-4843.

34. J. Stöhr, *NEXAFS Spectroscopy*, Springer, New York, 2003.

35. B. Ravel and M. Newville, *J. Synchrotron Radiat*. 2005, **12,** 537-541.

36. J. Zhou, J. Wang, H. Fang, C. Wu, J. N. Cutler and T. K. Sham, *Chem. Commun.* 2010, **46,** 2778-2780.

37. N. Severin, S. Kirstein, I. M. Sokolov and J. P. Rabe, *Nano Lett.* 2009, **9,** 457-461.

Energy & Environmental Science Accepted Manuscript

38. S. Royer and D. Duprez, *ChemCatChem* 2011, **3,** 24-65.

39. S. Aksel and D. Eder, *J. Mater. Chem.* 2010, **20,** 9149-9154.

40. I. K. Moon, J. Lee, R. S. Ruoff and H. Lee, *Nat. Commun.* 2010, **1,** 73-78.

41. S. H. Park, et al. *J. Mater. Chem.* 2011, **21,** 680-686.

42. Y. P. Wu, et al. *Adv. Mater.* 2013, **25,** 6744-6751.

43. S. Bhuvaneswari, et al. *Phys. Chem. Chem. Phys.* 2014, **16,** 5284-5294.

44. J. Y. Kim, et al. *Nanoscale* 2013, **5,** 6804-6811.

45. R. K. Mishra, et al. *Nanoscale* 2015, **7,** 11971-11979.

46. D. R. Dreyer, S. Park, C. W. Bielawski and R. S. Ruoff, *Chem. Soc. Rev.* 2010, **39,** 228-240.

47. H. Y. He, T. Riedl, A. Lerf and J. Klinowski, *J. Phys. Chem.* 1996, **100,** 19954-19958.

48. H. Kang, A. Kulkarni, S. Stankovich, R. S. Ruoff and S. Baik, *Carbon* 2009, **47,** 1520-1525.

49. B. R. Burg, J. Schneider, S. Maurer, N. C. Schirmer and D. Poulikakos, *J. Appl. Phys.* 2010, **107,** 034302-034307.

50. K. Sing, *Colloid. Surface A* 2001, **187,** 3-9.

51. A. Burke, *Electrochimica Acta* 2007, **53,** 1083-1091.

52. K. Parvez, et al. *ACS Nano* 2012, **6,** 9541-9550.

53. X. Li, et al. *J. Am. Chem. Soc.* 2009, **131,** 15939-15944.

54. H.-C.; et al. *ChemSusChem* 2015, **8,** 1875–1884.

55. B. J. Schultz, et al. *RSC Adv.* 2014, **4,** 634-644.

56. R. V. Dennis, et al. *J. Vac. Sci. Technol. B* 2013, **31,** 041204.

Energy & Environmental Science Accepted Manuscript

57. Y. Zubavichus, A. Shaporenko, V. Korolkov, M. Grunze and M. Zharnikov, *J. Phys. Chem. B* 2008, **112,** 13711-13716.
58. G. R. Iyer, J. Wang, G. Wells, M. P. Bradley and F. Borondics, *Nanoscale* 2015, **7,** 2289-2294.
59. Y. Chen, et al. Nanoscale Res. Lett. 2014, **9,** 646-653.
60. V. Lee, et al. *Phys. Chem. C* 2012, **116** 20591-20599.
61. V. Lee, et al. *Chem. Mater.* 2009, **21**, 3905-3916.
62. D. Pacilé, et al. *Carbon* 2011, **49,** 966-972.
63. H. Jeong, et al. *Europhys. Lett*. 2008, **82,** 67004-67008.

Author Information: The authors declare no competing financial interests. Correspondence and requests for materials should be addressed to K. B. K. (kbkim@yonsei.ac.kr) or K. C. R. (rkc@kicet.re.kr).

Acknowledgments: This work was supported by an Energy Efficiency and Resources program grant of the Korea Institute of Energy Technology Evaluation and Planning (KETEP) funded by the Ministry of Knowledge Economy, Korean government (No: 20122010100140). This research was supported by Basic Science Research Program through the National Research Foundation of Korea (NRF) funded by the Ministry of Education (2015R1A6A3A03018844). The work performed at Brookhaven National Laboratory was supported by the Assistant Secretary for the Energy Efficiency and Renewable Energy Office, Vehicle Technology, of the U. S. Department of Energy (DOE), under contract no. DE-SC0012704. Canadian Light Source is supported by the Canada Foundation for Innovation, the Natural Sciences and Engineering Research Council of Canada (NSERC), the University of Saskatchewan, the Government of Saskatchewan, Western

Energy & Environmental Science Accepted Manuscript

Economic Diversification Canada, the National Research Council Canada, and the Canadian Institutes of Health Research. We greatly thank the kind help from Dr. Tom Regier, beamline scientist at SGM beamline at CLS.

Author Contributions: H. Kim designed, oversaw and participated in all steps of the experiment and in writing and editing the manuscript. S. Lee, M. Kim, Y. Choi, J. Han, K. Chung, and K. Nam participated in analyzing the structure and electrochemical properties of the samples and provided feedback on the manuscript. S. Bak, J. Wang, J. Zhou, X. Yang performed NEXAFS and STXM analyses and partially participated in writing and editing the manuscript. B. Park, S. Lee and S. Jun participated in analyzing the electrical conductivity and optical properties of the samples. K. Roh and K. Kim reviewed and commented on the manuscript. All authors discussed the results and commented on the manuscript.

Energy & Environmental Science Accepted Manuscript

Figure legends

Figure 1. Catalytic metal oxide (SnO_2) nanoparticles were deposited on the GO surface (partially reduced GO, RGO) at 25°C with stirring. Next, the composites were subjected to controlled air oxidation via heating in an open-ended tube furnace. Finally, the partially oxidized RGO sheets were refluxed at 80℃ with diluted acid for 4 h to produce GNMs. Scale bars, 10 nm.

Figure 2. (a) TEM images (scale bar, 500 nm), (b) (scale bar, 100 nm), (c) HR-TEM images (scale bar, 20 nm), (d) Cs-corrected TEM image and FFT diffraction patterns of GNMs (scale bar, 10 nm and 5 1/nm)). The perforations are 5–10 nm and are on the micron scale. RGO nanosheets and GNM sheets retained a highly crystalline graphitic structure after nanoperforation except in the nanoperforated areas. (e) AFM image and height profile diagram of GNM. The height profile diagram indicates the size of the perforations on the graphene oxide sheets.

Figure 3. (a) L-GNMs (b) GNMs, and (c) H-GNMs (scale bar, 20 nm) from 7 wt.% SnO_2-RGO, 11 wt.% SnO_2-RGO, and 17 wt.% SnO_2-RGO. (scale bar, 50 nm)

Figure 4. (a) XRD patterns, (b) XPS survey spectra (c) NMR spectra, and (d) Raman spectra of GO, SnO_2-RGO, and GNM. All of the results confirm efficient de-oxygenation of GO in the as-prepared GNMs. Compared with the parent GO, the GNM peaks were dramatically upshifted, suggesting that they were well-ordered with two-dimensional sheets and that there was a decrease in the average interlayer spacing. XPS showed that the C/O atomic ratio was 1.9 for GO and 10 for the GNM. The NMR spectra show the graphitic C sp^2 peaks of GO (127.75 ppm), SnO_2-RGO (116.35 ppm), and GNM (110.50 ppm). The higher D/G ratio in the Raman spectra

Energy & Environmental Science Accepted Manuscript

and the greater weight loss observed for the GNMs compared with GO were attributed to defects and oxygen functional groups around the nanoperforations in the GNMs.

Figure 5. (a) Cyclic voltammograms of GNMs at 1–1000 mV s^{-1}. (b) Galvanostatic charging–discharging profiles at a current density of 1–20 A g^{-1} for P-graphene and GNMs. (c) Rate capabilities of P-graphene and GNMs at various current densities between 1 and 100 A g^{-1}, where the specific capacitance of each sample was calculated from the associated galvanostatic discharge results. Electrochemical impedance spectroscopy results related to the (d) Nyquist plots and (e) Bode plots for P-graphene and GNM (f) cyclability of GNM.

Figure 6. (a) Full-scale and (b) C 1s XPS spectra of N-GNMs prepared by NH_3 gas treatment of GNMs at 900 ℃ ; (c) C K-edge NEXAFS spectra and (d) oxygen K-edge NEXAFS spectra with pre-edge normalization ; (e) N K-edge NEXAFS spectra for GNMs and N-GNMs.

Energy & Environmental Science Accepted Manuscript

Figure 1.

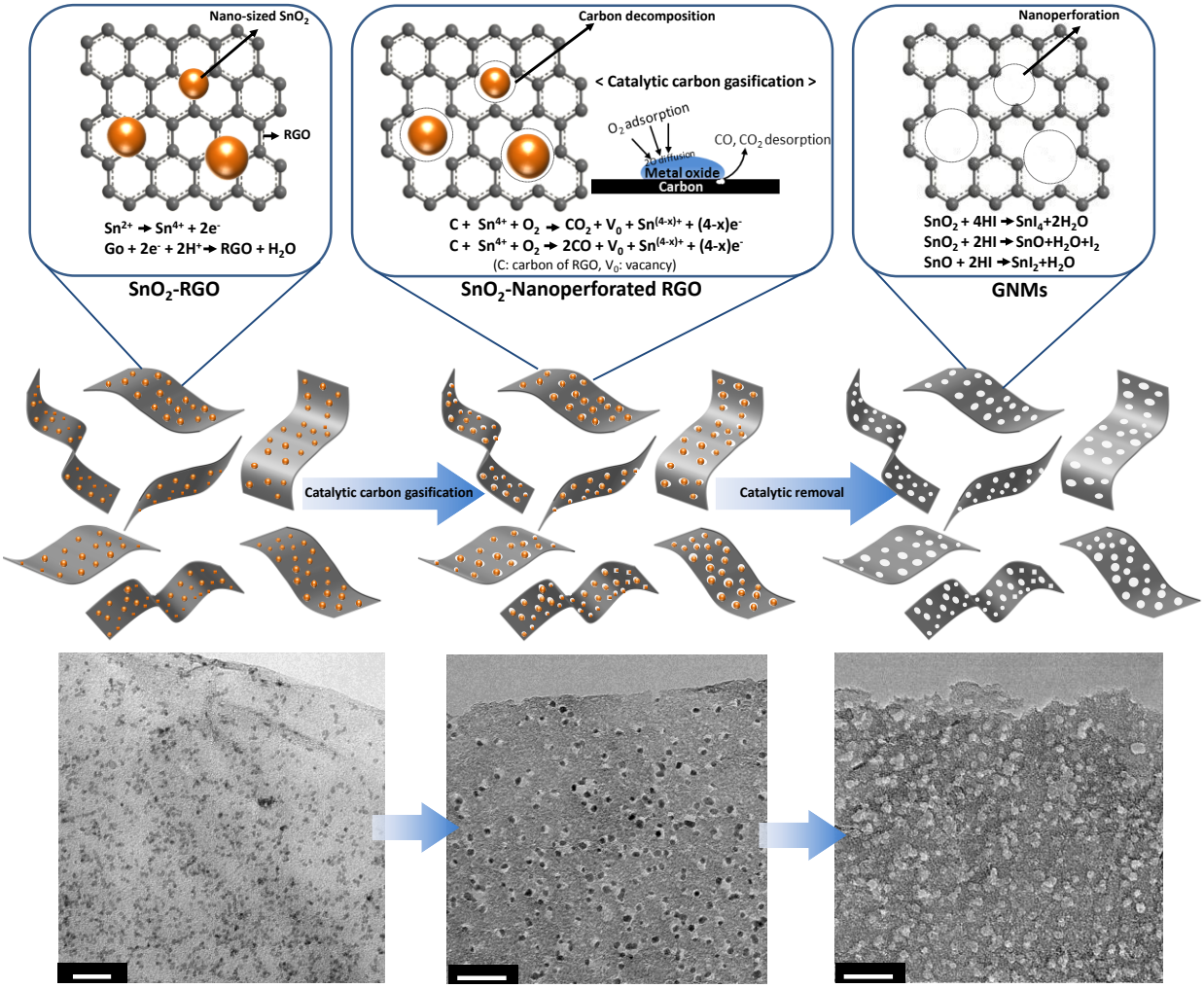

Energy & Environmental Science Accepted Manuscript

Figure 2.

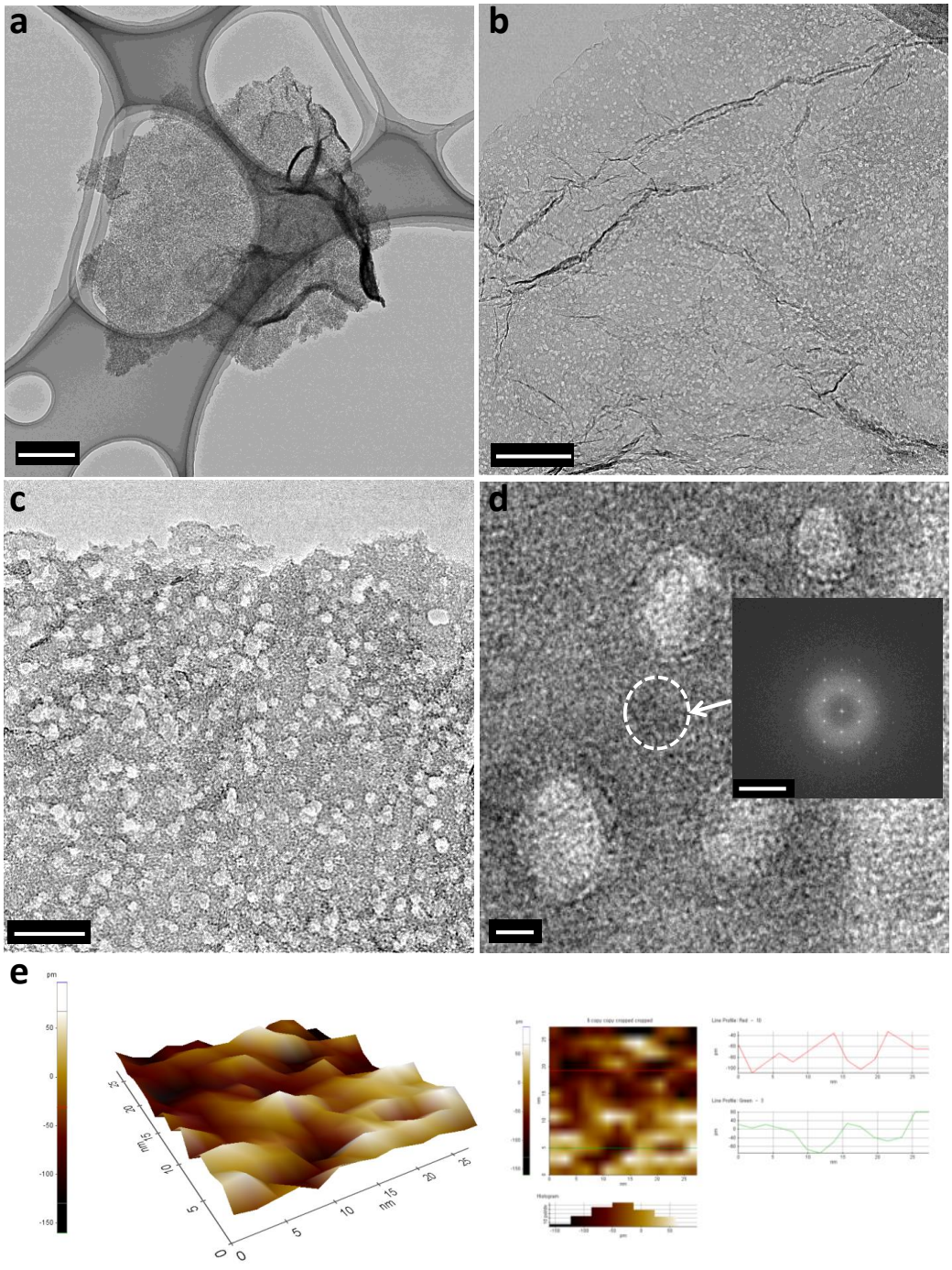

Energy & Environmental Science Accepted Manuscript

Figure 3

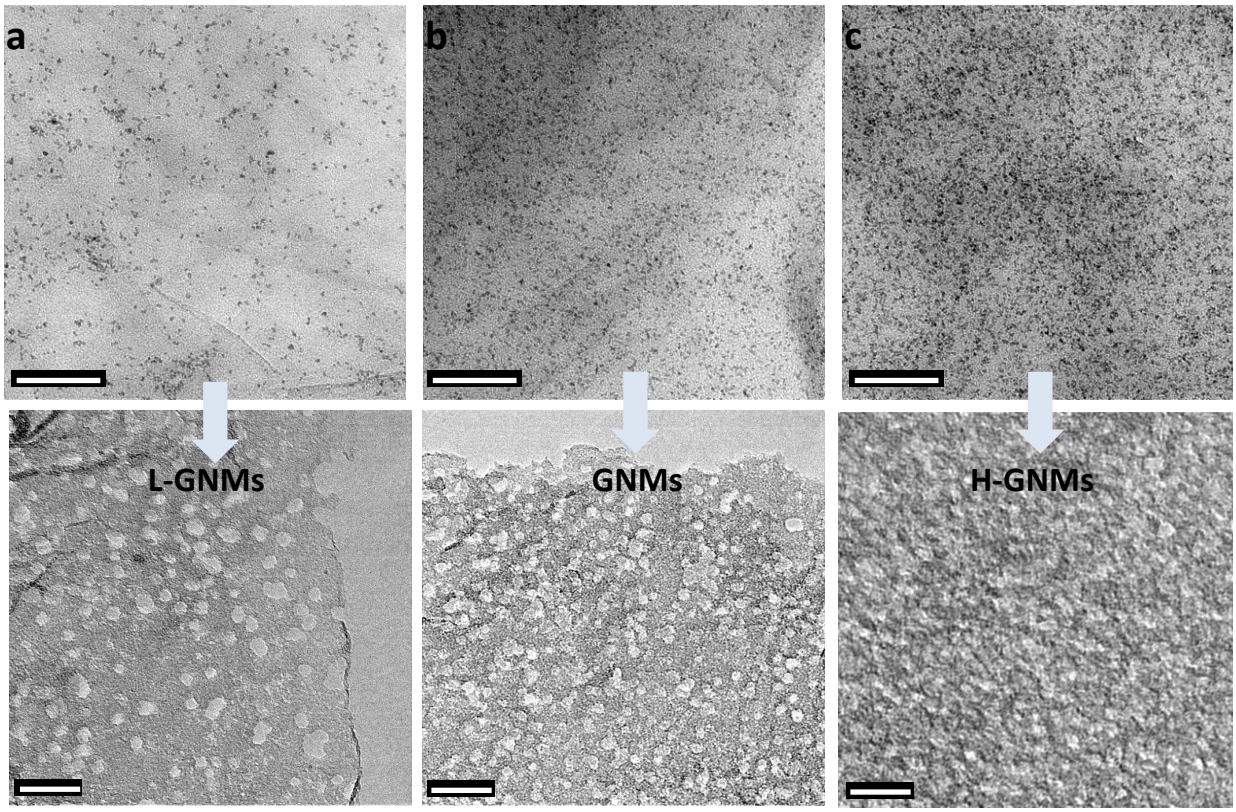

Energy & Environmental Science Accepted Manuscript

Figure 4.

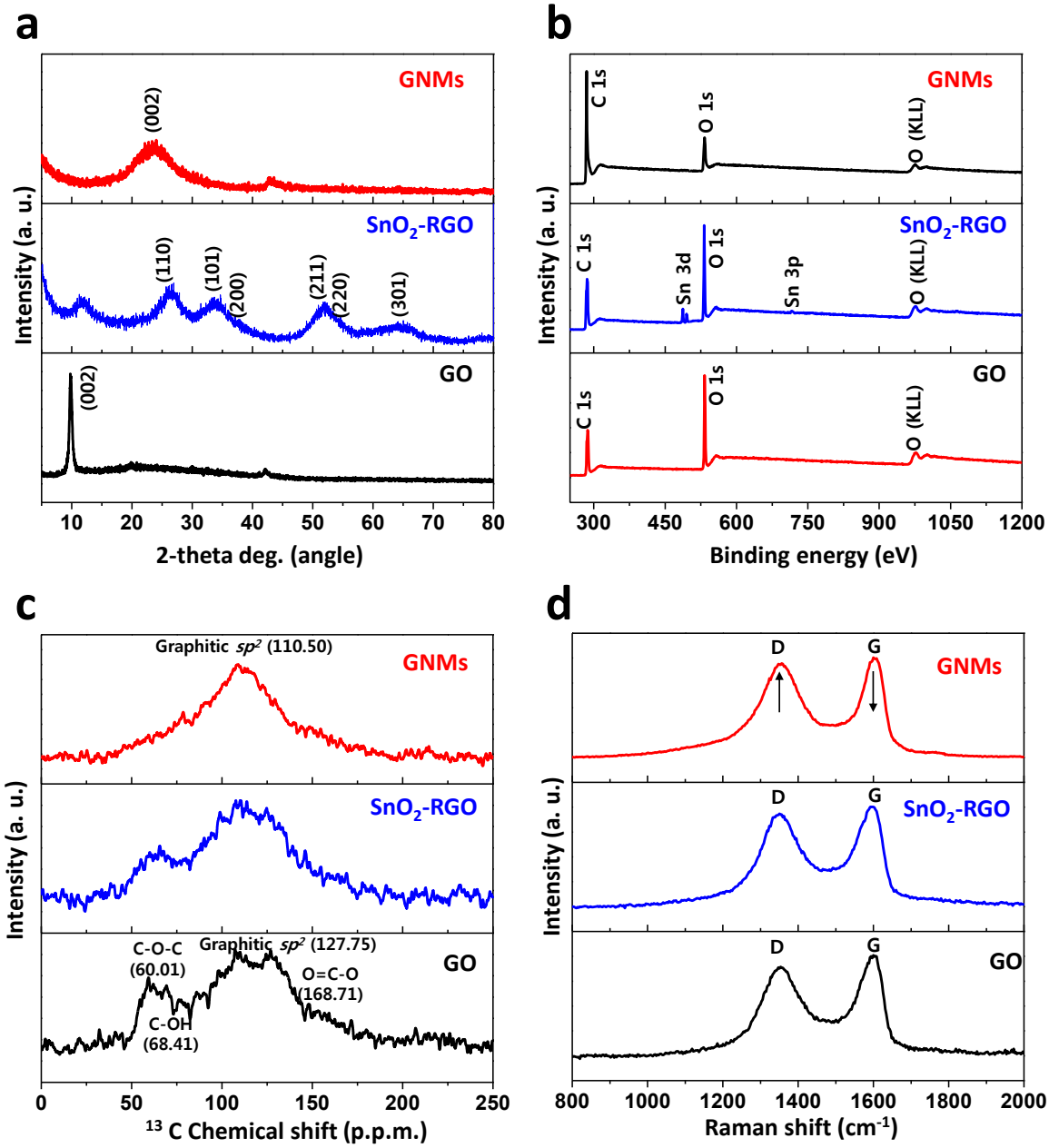

Energy & Environmental Science Accepted Manuscript

Figure 5.

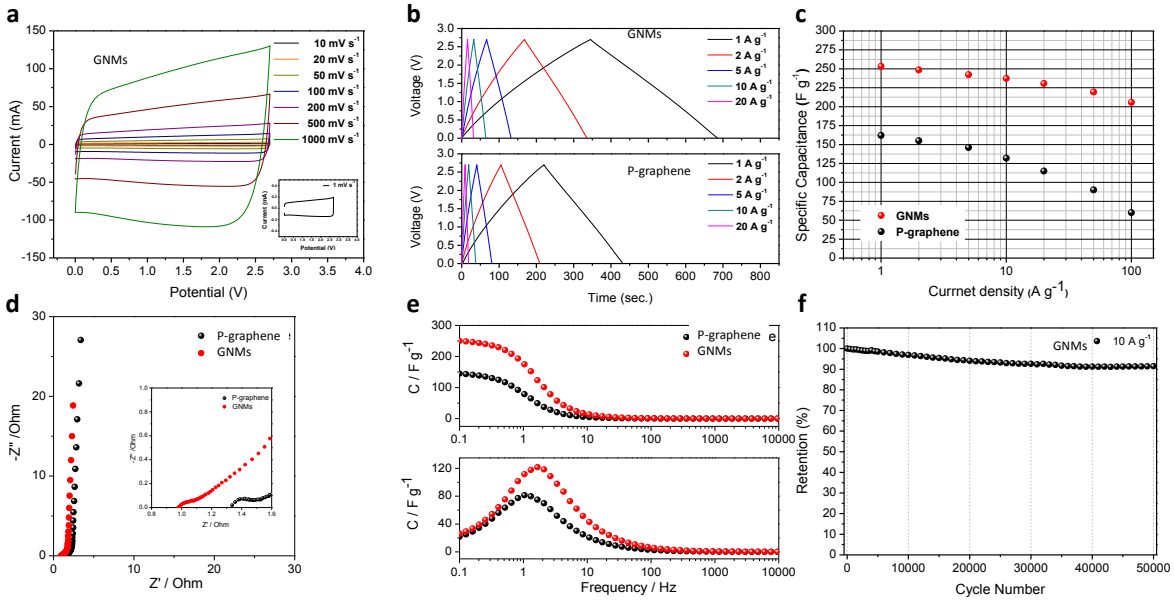

Energy & Environmental Science Accepted Manuscript

Figure 6.

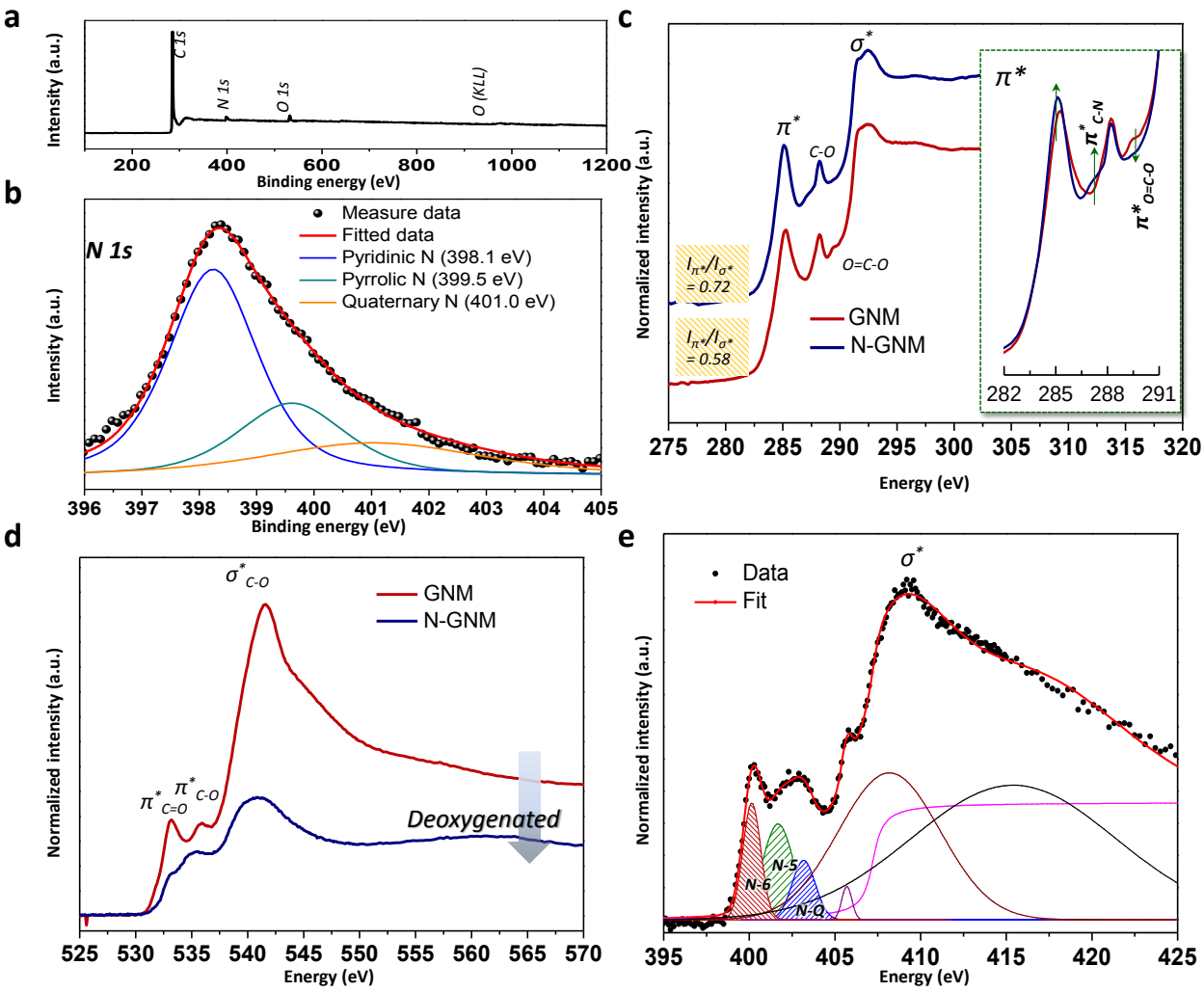

Energy & Environmental Science Accepted Manuscript